PHYSICAL REVIEW B **109**, 195106 (2024)

Transport spectroscopy study of minibands in MoS_2 moiré superlattices

Chithra H. Sharma,[1,2,*] Marta Prada,[3,†] Jan-Hendrik Schmidt,[1] Isabel González Díaz-Palacio,[1] Tobias Stauber,[4]
Takashi Taniguchi,[5] Kenji Watanabe,[6] Lars Tiemann,[1] and Robert H. Blick[1,7]
[1]*Center for Hybrid Nanostructures (CHyN), Universität Hamburg, Luruper Chaussee 149, Hamburg 22761 Germany*
[2]*Institut für Experimentelle und Angewandte Physik, Christian-Albrechts-Universität zu Kiel, Leibnizstrasse 19, 24098 Kiel, Germany*
[3]*I. Institute for Theoretical Physics, Universität Hamburg, Luruper Chaussee 149, Hamburg 22761 Germany*
[4]*ICMM-CSIC, Sor Juana Inés de la Cruz 3, Madrid 28049 Spain*
[5]*International Center for Materials Nanoarchitectonics, National Institute for Materials Science, 1-1 Namiki, Tsukuba 305-0044, Japan*
[6]*Research Center for Functional Materials, National Institute for Materials Science, 1-1 Namiki, Tsukuba 305-0044, Japan*
[7]*Material Science and Engineering, University of Wisconsin-Madison, University Ave. 1550, Madison 53706, Wisconsin, USA*

(Received 29 August 2023; accepted 2 April 2024; published 1 May 2024)

The exotic correlated phases that emerge in the low-dispersing moiré bands of twisted van der Waals structures have opened new exciting opportunities in condensed-matter physics. These systems exhibit a rich phase diagram of novel physical phenomena and exotic correlated phases that emerge in the low-dispersing bands. Despite its popularity, the resulting mini-bands in the conduction band of MoS_2 moiré superlattices remained elusive so far. In this work, we resolve these spin-valley mini-bands via transport spectroscopy in micron-scale devices. The theoretical energy scales exhibit an astounding agreement with our experimental observations, which together with the behavior under thermal activation, suggest an electronic phase transition. These intriguing observations highlight the potential of twisted MoS_2 structures as a playground to explore correlated electron states and associated phenomena.

DOI: 10.1103/PhysRevB.109.195106

I. INTRODUCTION

The periodic potential of a crystal structure induces bands of allowed energies that ultimately determine the physical properties of a solid. The placement of two van der Waals (vdW) layers under a specific rotation angle leads to a moiré superlattice (MSL), resulting in unexpected physical properties. The first observations of these "magic" changes to the physical properties were made in twisted bilayer graphene that suddenly exhibited a sequence of correlated insulating [1], superconducting [2,3], and ferromagnetic phases [4,5] as a result of the reconstruction of the energy dispersion at the magic angle of ≈1.05° [6]. It is a general consensus that a reconstruction of the energy dispersion flattens the electronic bands, essentially turning massless Dirac fermions into heavily interacting particles [6]. These discoveries in graphene triggered a run to the extended family of vdW transition metal dichalcogenides (TMDCs) [7–15] where the stringent magic angle condition for flat-band formation is relaxed [9,10]. It did not take long until experimental reports of Mott insulating phases [8] followed for magic angle TMDCs.

The attention has recently turned to flat-band related phenomena at zero magnetic field, where spontaneous symmetry breaking [16] causes a cascade of Lifshitz transitions [17–19], observed in bilayer graphene as the spin and valley degeneracy are spontaneously broken at integer moiré band filling. Owing to the low spin-orbit coupling (SOC) ensuring quasidegenerate states [20], an attractive TMDC candidate to observe these phenomena is the conduction band of twisted MoS_2 structures [21]. Although the moiré bands were theoretically predicted [12,13], the MSL in MoS_2 is unexplored in electronic transport experiments. Here, we resolve the discrete spin-valley mini-bands in MSLs of twisted MoS_2 via transport spectroscopy by taking advantage of the tunneling across the Schottky barriers (SBs). Two independent observations from our experiments support that the signatures we measure are related to a phase transition triggered by correlations: (i) The mini-bands appear only at temperatures below the spin-valley gap (<10 K), allowing spontaneous flavor polarization (ii) Absence of mini-bands in large angle and nontwisted samples.

In this work we consider a twisted bilayer MoS_2 (tBLM); device A, and two twisted double-bilayer MoS_2 (tDBLM); devices B and C. The schematics of the device and experimental circuiting is depicted in Fig. 1(a), whereas Fig. 1(b) shows a cartoon of the MSL in MoS_2. The devices are encapsulated in hBN and, a graphite flake at the bottom works as the gate-electrode. More fabrication details are presented in Appendix A. Figure 1(c) shows a false-colored SEM image of device A. The perimeter of the lower and upper monolayers MoS_2 flakes are marked with green and pink dashed lines, respectively. The angle θ between the straight edges is then deduced from these optical images, where the long straight edges of the flakes are assumed to be zigzag; the preferable cleavage direction for MoS_2 [22,23]. We measure θ to be 4.40°, 6.22°, and 1.21°, respectively for devices A, B, and C.

---

[*] Chithra.Sharma@physik.uni-hamburg.de

[†] mprada@physnet.uni-hamburg.de

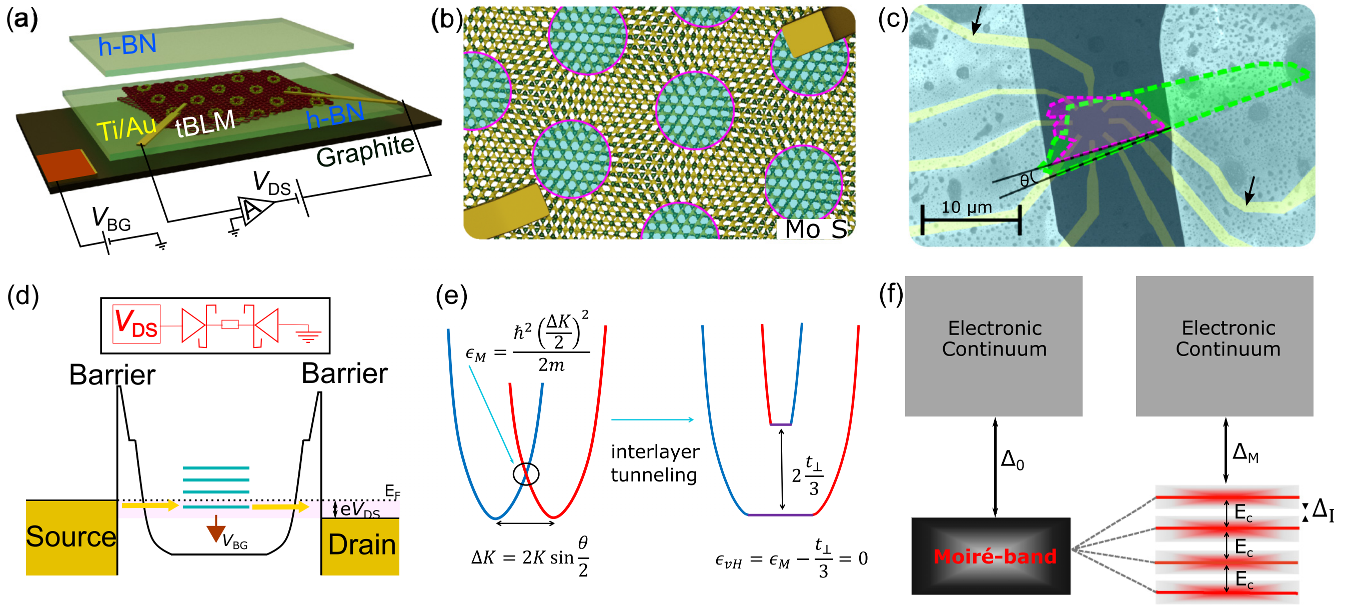

FIG. 1. (a) Schematics of the sample configuration with the moiré superlattices encapsulated in hBN. (b) Cartoon showing the atomic arrangement of a twisted bilayer MoS_2, with AB stacked domains marked in pink circles. (c) False-colored SEM image of the device with the two MoS_2 flakes outlined in green and pink for clarity. The two contacts (source and drain) used for the measurement are marked with black arrows (see Appendix A for more details). (d) A level diagram illustrating transport via discrete moiré mini-bands. The inset shows an equivalent circuit diagram with the Schottky contact represented as a diode. (e) Energy dispersion and (f), band diagrams illustrating the band hybridization near the magic angle or flat-band condition (left) and the spontaneous spin-valley symmetry breaking that emerges with interactions (right).

Owing to the point-group symmetry of MoS_2, we may assume a twist angle of θ or $60^\circ \pm \theta$ (see Appendix B for details).

The Ti/Au contacts, marked by golden stripes in Fig. 1(c) exhibit Schottky behavior and poses challenge for electrical transport [24,25]. We model the Schottky contacts as diodes symmetrically connected as in the circuit representation shown in the top-inset of Fig. 1(d). However, we exploit the quantum-mechanical tunneling through the barrier to resolve the discrete MSL mini-bands. A simple model for the mini-band formation is elaborated in Sec. II A and the transport model for barrier tunneling on which our analysis is based on is explained in Sec. II B. Our experimental results and analysis are detailed in Sec. III.

II. THEORETICAL BACKGROUND

A. Theoretical model for mini-band formation

We consider a simple model explained below that considers the lifting of spin and valley degeneracy in the magic-angle moiré band, as observed in graphene-based structures [17–19,26–29] and twisted bilayer TMDCs [8] as a hypothesis to explain our experimental data discussed in the following section.

The normally fourfold degenerate conduction band of the individual layers that form the moiré system has a parabolic dispersion $\epsilon(\mathbf{k}) = \hbar^2k^2/2m$, where $m = 0.76m_0$ with m_0 being the free-electron mass [30]. Due to the twist angle, the minima of the parabolic dispersion of the two layers are separated by the wave vector $\Delta K = 2K\sin(\theta/2)$, where $|\mathbf{K}| = K = 4\pi/3a$ as shown in the left of Fig. 1(e) [30]. The parabolic bands of the upper and lower layer anticross at the so-called moiré energy $\epsilon_M = \epsilon(\Delta K/2)$. Band hybridization via interlayer hopping $t_\perp \simeq 40$–50 meV [31,32] results in spin and valley degenerate bonding and antibonding states, as shown schematically on the right-hand side of Fig. 1(e). The magic angle condition reads [33]

$$\epsilon_M - \frac{2t_\perp}{3} = 0. \tag{1}$$

Here, the gap enhancement owing to lattice relaxation is accounted for by adding a factor of two above [34,35]. This gives a magic angle of

$$\theta_M \simeq \frac{3a}{2\pi}\sqrt{\frac{2m}{\hbar^2}\frac{t_\perp}{3}} \approx 4^\circ\text{–}5^\circ.$$

Near the magic angle, the single-particle spectrum of the low SOC conduction band can thus be approximated by a valley and spin fourfold degenerate ground-state that forms a mini-gap of $\Delta_M \simeq 2t_\perp/3$ with the continuum.

In the presence of interactions, this fourfold degeneracy is broken [36]. Simple order of magnitude arguments show that the leading electron-electron interaction in the system is the long-range Coulomb interaction. This gives an estimate of the Coulomb energy to be of the order of $E_c = e^2/(4\pi\epsilon\epsilon_0 L) \simeq 40$–$50$ meV, where ϵ_0 is the permittivity of free space, the dielectric constant, $\epsilon \simeq 4$–6 is the screening from the hBN environment [37] in our samples and $L \sim a/2\sin(\theta_m/2) \approx 5$ nm [38], with $a = 0.319$ nm being the lattice constant. At integer moiré band fillings, the electron-electron interaction results in incompressible states [17], causing Lifshitz phase transitions and a band structure as schematically depicted in Fig. 1(f). Whenever the occupation per moiré cell reaches an

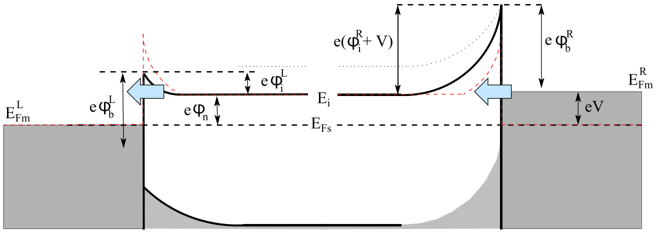

FIG. 2. Cartoon illustrating transport in reverse bias mode.

integer value, the corresponding virtually occupied channel splits up by the Coulomb energy E_c.

B. Theoretical transport model for barrier tunneling

At low temperatures, the dominant mechanism for current transport is found to be field-emission tunneling [39]. This occurs in particular when the Fermi energy of the contact levels the moiré flat band, which is centered around an energy E_i.

We employ a Landauer formalism to account for the tunneling current through the reverse-operating device:

$$I \simeq e \int_0^\infty v_x \Gamma(E) \mathrm{DOS}(E) e^{-(E-E_{Fs})/k_BT} dE$$

$$= I_0(T) \int_0^\infty \Gamma(E) \mathrm{DOS}(E) e^{-(E-E_{Fs})/k_BT} dE, \quad (2)$$

where v_x is the velocity of electrons along x, density of states DOS is the density of states, and Γ is the transmission over the barrier of height $e\phi_b^R$ (see the cartoon in Fig. 2) [40].

We assume a triangular barrier for the Schottky contact [41] within the WKB approach,

$$\Gamma(E) \propto \exp\left[-(e\phi_i + eV - E)/E_0\right], \quad (3)$$

with the basis given by $d \simeq \sqrt{2\epsilon_s \phi_b / q n_d}$, where ϵ_s is the dielectric constant and n_d the donor concentration. For a triangular barrier within the WKB approach via quasidiscrete levels E_i, we have

$$\Gamma(E)\mathrm{DOS}(E) \sim \exp\left\{\frac{-8\sqrt{m^* \epsilon_s}\phi_b}{3q\hbar\sqrt{n_d}}\right\} \delta(E - E_i), \quad (4)$$

where m^* is the effective mass of MoS_2. We perform direct integration with two parameters, I_0 and ϕ_i^R to fit the experimental data. To mimic the finite dispersion of the moiré level E_i, we employ a Breit-Wigner function [42],

$$\delta(E - E_i) = (1/2\pi)\gamma / [(E - E_i)^2 + (\gamma/2)^2], \quad (5)$$

resulting in the DOS obtained in Sec. III. Note that for the contribution of the continuum (at higher voltages) we have $\mathrm{DOS}(E) = n_{2d}$, which is the density of electrons in the two-dimensional electron gas.

The effects of the gate are then included by shifting the energy scale on the DOS by $e\alpha V_{BG}$, where α is a rational function of the capacitance of the system [43]. We extract $\alpha = 0.025$, which is reasonable for a gate distance of 27 nm. The theoretical fits for our experimental data below are obtained by numerical integration of equation (2), where the only free parameter is the barrier height ϕ_i.

III. TRANSPORT MEASUREMENTS AND ANALYSIS

Two-probe measurements were performed on the devices by applying a DC drain-source bias voltage V_{DS} and measuring the current I_{DS} via a current pre-amplifier [see Fig. 1(a)]. We apply a DC voltage at the graphite back-gate (V_{BG}) to shift the Fermi level through the discrete mini-bands. We exploit the negative differential conductance (NDC) induced by the SBs at the electrical contacts to resolve four mini-bands arising from the spin-valley symmetry breaking and corresponding energy gaps in the proximity of the conduction band of twisted MoS_2 structures. Device A was measured at 4.2 K and devices B and C at 1.5 K, unless stated otherwise.

A. Low-temperature transport in twisted bilayer MoS_2

The I-V characteristics for device A ($\theta = 4.40^\circ$) in reverse (negative) bias operation are shown in Fig. 3(a) for selected gate voltages above the on-state, $V_{BG} > 3$ V. The solid lines are experimental data, whereas the dashed lines correspond to theoretical fits (see Sec. II B). Below $|V_{DS}| < 20$ mV, the turn-on voltage, negligible current flows through the device. Increasing $|V_{DS}|$ boosts the tunneling current [41], as bands are shifted into the conducting window near the Fermi level. The four step-like structures in Fig. 3(a) with increasing bias reveal the discrete nature of the moiré bands below the conduction band [12,13,44]. As the gate voltage increases, the MSL levels shift down in energy [see diagram in Fig. 3(d)], lowering the bias threshold $|V_{DS}|$. The steps shift linearly with V_{BG}, indicating that, for small biases used here, the gate affects the levels homogeneously and independently of the barrier. Note that such a linear shift is typically observed in resonant tunneling transistors [45,46].

A salient feature of Fig. 3(a) is the observation of an NDC region following each step in the I-V curve. A possible explanation would be that the bias increases the SB height [47] while no new states become available for conduction, resulting in NDC. If we assume correlation effects, it would also show NDC, owing to the formation of a bound state [48,49], which is sensitive to temperature [50]. We stress that these features are absent in nontwisted samples. Appendix C shows optical image and I-V measurements from a few-layer MoS_2 device with similar architecture and measured in same setup for various V_{BG} at 4.2 K, ruling out the possibility of a measurement artifact.

Employing a simple Landauer formalism and assuming a Breit-Wigner DOS, we were able to fit the experimental data [broken lines of Fig. 3(a)]. A plot of the extracted DOS as a function of V_{DS} is shown in Fig. 3(b). See Sec. II B for details. The theoretical Coulomb energy $E_c \sim e^2/(4\pi\epsilon\epsilon_0 L) \approx$ 40–50 meV that we deduced from a first approach calculation (see Sec. II A) is strikingly close to the corresponding V_{DS} separation of the steps observed in Fig. 3(a). From the extracted DOS [Fig. 3(b)], we obtain a charging energy of $E_c \simeq (32 \pm 2)$ meV and a mini-gap of $\Delta_M \simeq (38 \pm 5)$ meV. Our Δ_M compares favorably with the value experimentally obtained for graphene [1] and theoretically for MoS_2 [13].

Figure 3(c) shows a contour plot of I_{DS} as a function of V_{DS} and V_{BG}. The emergence of clear plateaus in the current allows us to resolve discrete levels labeled by 1 through 4.

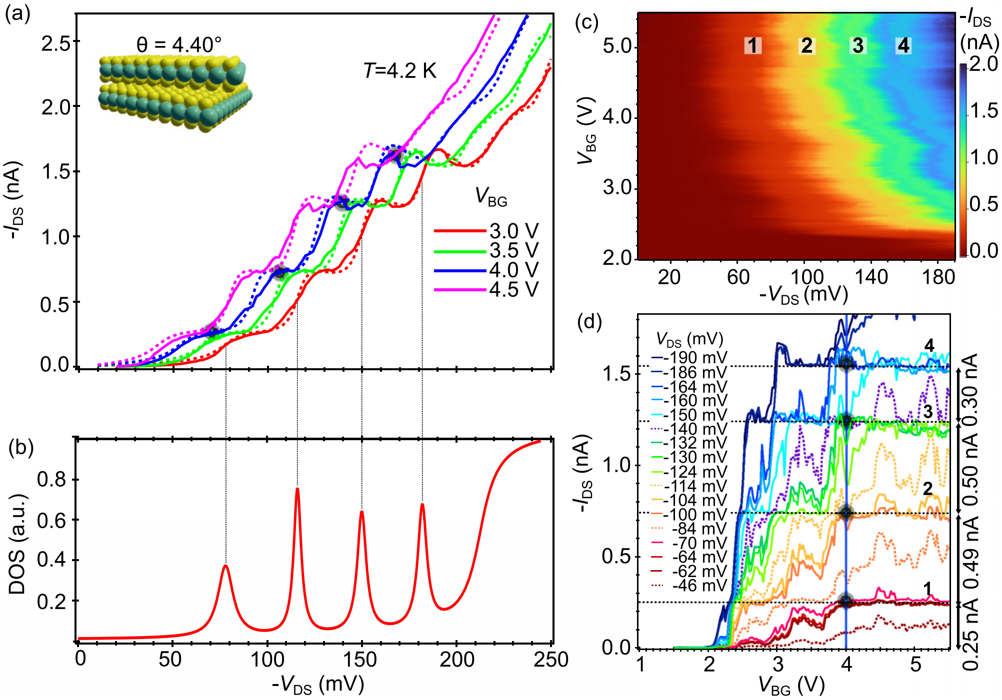

FIG. 3. Resonant tunneling and negative differential conductance in tBLM (device A). (a) Experimental *I-V* traces (solid lines) and theoretical fits (dashed) for different back-gate voltages, V_{BG}. (b) DOS extracted (see Sec. II B) from the *I-V* traces, plotted for $V_{\mathrm{BG}} = 3$ V. (c) A contour plot of the current as a function of V_{DS} and V_{BG} depicting the four plateaus. (d) I_{DS} as a function of V_{BG}, showing step-like, nonlinear behavior for different V_{DS}. A blue vertical line at $V_{\mathrm{BG}} = 4$ V corresponds to the blue curve in panel (a) and the black dots on both plots correspond to the plateau regions with the same parameters. Horizontal lines are guides to the eye for values where the current flattens.

These four clear plateaus in the current are evidence of a nontrivial energetic spectrum. We stress, however, that the SB prevent us from extracting the conductance in quantized units of e^2/h. Figure 3(d) shows line cuts with the current as a function of V_{BG} at different V_{DS}. The blue vertical line at $V_{\mathrm{BG}} = 4$ V corresponds to the blue curve in the top panel of Fig. 3(a) and the black dots on both plots correspond to the plateau regions with identical parameters. The current flattens to four well-defined values of separation (0.25 ± 0.02), (0.49 ± 0.02), (0.50 ± 0.02), and (0.30 ± 0.02) nA, for particular windows of drain-source and gate voltages, marked by the horizontal lines (guides to the eye). Remarkably, the current exhibits a larger amount of noise for drain-source bias between these windows (in dashed lines), and well-defined, low noise values for bias within the windows. See Appendix D for the noise spectra extracted from the data. The second and third steps show roughly an increment of twice the step size as the first and fourth. We speculate that this could be related to the nature of the different broken symmetries (spin and valley), or the nontrivial connection of the bands [16]. A deeper theoretical analysis beyond this experimental work would be needed to unravel further details of this low-noise region and the different shapes of the even and odd steps.

B. Temperature dependence in twisted bilayer MoS$_2$

Figure 4(a) shows the temperature dependence of the *I-V* characteristics at $V_{\mathrm{BG}} = 4$ V. We note that there are two relevant energy scales involved in our transport experiments. (i) The Schottky barrier height (order of ≈10 meV) leads to the observation of the moiré band as a shoulder in the *I-V* curves up to 80 K. Above 80 K, the feature is washed out as k_BT overcomes the SB height, where the linear approximation breaks down. (ii) The single-particle spin and valley splitting

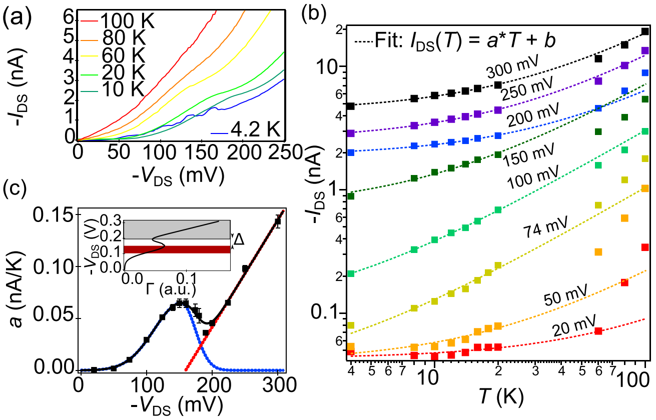

FIG. 4. (a) Experimental *I-V* traces of device A for different temperatures at $V_{\mathrm{BG}} = 4$ V and (b) Log-log plot of the current as a function of temperature for different biases. The linear fit (broken lines) to the experimental data (squares) is well suited at low temperatures, $T \lesssim 20$ K. (c) The linear coefficient a (related to the transmission coefficient, Γ) which is sensitive to the sample's DOS plotted against V_{DS}: The peak at ≈150 mV relates to the moiré band, whereas the linear increase corresponds to the constant DOS or the electronic continuum in the two-dimensional system, as illustrated in the inset.

within the fourfold moiré band (<1 meV) [36,51] results in the steps visible only below ≈10 K. (dark blue trace). It is thus only below 10 K that interactions can lift the flavor degeneracies and give rise to a phase transition [19], yielding valley-polarized bands with interaction-induced gaps of the order of E_c. This serves as an upper bound to the energy scale to observe the correlated state, $\lesssim$0.86 meV, and agrees with that of bilayer graphene [7,36,51]. We note that the sample was recooled for the temperature-dependent measurements. Consequently, an increase in the SB causes the crossing of the blue and green curves at low bias voltages.

The current as a function of temperature for different biases is depicted in Fig. 4(b) employing a log-log scale. At low temperatures, $T \lesssim 20$ K, the current increases linearly with temperature, $I_{DS} = a(V_{\rm DS})T + b$, a common feature of tunneling through SB [41]. The dashed curves correspond to the linear fit, whereas the filled-squares are experimental data points. The extracted linear coefficient is represented as a function of $V_{\rm DS}$ in Fig. 4(c). Two regimes can be distinguished: A Lorentzian around 160 mV (blue broken curve), corresponding to the Breit-Wigner shaped DOS of the moiré band, and a linear increase (red line), which can be identified with the constant DOS of the electronic continuum. Note that $a(V_{DS})$ is closely related to the quantum transmission coefficient of electrons below the barrier (see Sec. II B for details) as shown in the inset. The black curve corresponds to the total transmission, which is the sum of the red and blue traces.

C. Transport in twisted double-bilayer MoS$_2$

Next, we consider two double-bilayer structures. The *I-V* characteristics in reverse (negative) bias operation at positive back-gate voltages and gate sweep are shown in Figs. 5(a) and 5(b) (device B) and in Figs. 5(c) and 5(d) (device C). The main difference between these two samples is the relative angle between the top and bottom bilayer, which is 6.22° for device B and 1.21° for device C. The solid lines are experimental data, whereas the dashed lines correspond to a theoretical fit (see Sec. II B). While only one mini-band is resolved for device B, device C shows a set of mini-bands. This is consistent with the picture where a larger MSL (smaller angle) causes the favorable stacking region to occupy the largest area, lowering the symmetry of the MSL and favoring the appearance of moiré bands with larger confinement [13]. Note that, in contrast with device A, devices B and C have larger $I_{\rm DS}$ and the shift in the steps in *I-V* as a function of $V_{\rm BG}$ shows a nonlinear trend. This could be related to the nonuniformity of the vertical current flowing through a multiple-layered structure [52], preventing us to resolve the mini-gaps for some bias. However, we determine a Coulomb energy of $E_{\rm c} \simeq (22 \pm 4)$ meV, which is consistent with the larger MSL structure. Note that the scaling law of the Coulomb interaction is nontrivial, owing to the intricacies of the atomic reconstruction [53].

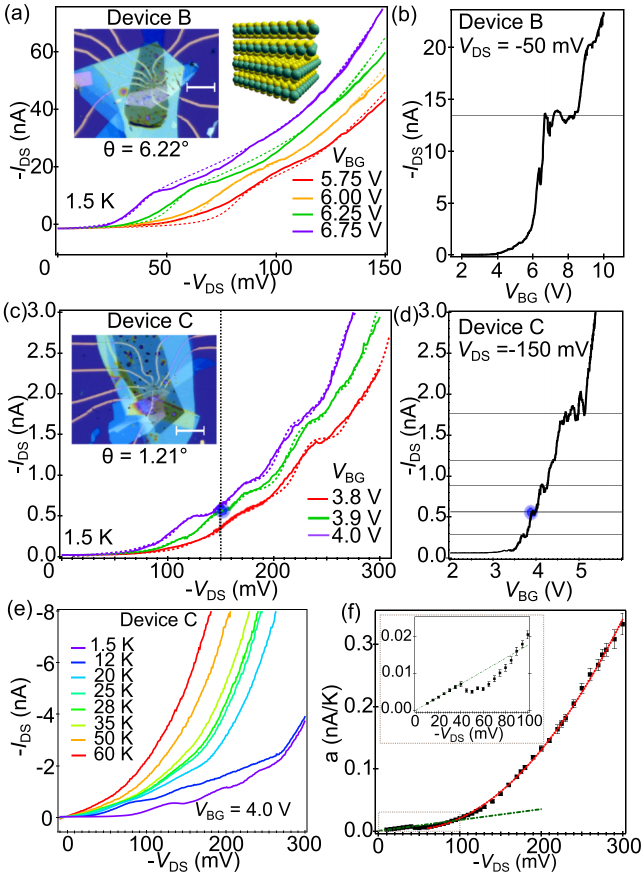

FIG. 5. (a), (c) *I-V* characteristics for different $V_{\rm BG}$ for devices B and C. The optical images of the respective devices are shown in the insets. The scale bar is 20 μm. (b), (d) Current as a function of back-gate voltage, showing step-like, nonlinear behavior of devices B and C. The right inset in panel (a) depicts the double-bilayer structure. The black horizontal lines in panel (d) correspond to the plateau regions and the blue dots in panels (c) and (d) correspond to the same parameters. (e) Temperature dependence of the *I-V* characteristics for device C. (f) Linear coefficient extracted from the temperature dependence as in Fig. 4(c).

To discriminate the nature of the features of Fig. 5(c), we evaluate the *I-V* characteristics as a function of the temperature. As we can see in Fig. 5(e), the features disappear around 25 K. We observe a linear behavior of the transmission with temperature up to 60 K, revealing a higher energy scaling of the SB. The coefficient *a* [Fig. 5(d)] shows also a nonmonotonic behavior at around 50 meV, which we identify with the moiré band. This behavior is consistent with the observation of temperature dependence in device A. This is a strong indication that the origin of the mini-bands is indeed due to the breaking of the spin-valley degeneracy.

IV. CONCLUSIONS

We present here an observation of the conduction minibands in the MSLs of MoS$_2$ and first report of the correlation-driven spin-valley symmetry breaking and resulting electronic transition in a TMDC putting MoS$_2$ in the road map of twistronics and associated correlation-driven phenomena. While the formation of Schottky contacts in MoS$_2$ is considered unfavorable in transport measurements, we harness the same to resolve the four discrete energy levels separated by ≈32 meV in the conduction band of twisted bilayer

MoS_2 devices. Unlike conventional spectroscopy techniques used to probe them locally, we show that the mini-bands and phase transitions can be observed and addressed in micron-scale devices spanning over a million moiré unit cells. In spite of the large gaps, the steps in the *I-V*s could only be observed at very low temperatures. The predicted localization of electrons at a specific stacking in the MSL potentially leads to the formation of mini-bands in the CB [13]. However, this explanation does not account for the observed temperature dependence in our experiments. Our simple model of electronic phase transition driven by spin-valley symmetry breaking and deduced energy levels agrees with all our experimental observations making it a potential origin for the observed the mini-bands. The low SOC in the conduction band of MoS_2 facilitates the phase transition at zero magnetic field, implying a quasi-fourfold degeneracy of the charge carriers. Such phase transitions had thus far only been observed in magic-angle twisted bilayer graphene [17–19]. These states, whose exact origin and their interplay with electronic correlations are yet unclear, are considered to host the exotic correlated states emerging in these systems [1,19] and makes MoS_2 a strong candidate for the study of correlation-driven phenomena. We also observe similar features in twisted double-bilayer structures consistent with our inferences. We believe that our results motivate further experiments on MSLs of MoS_2. Also, we could not characterize the states in terms of symmetry broken states (valley coherent, valley polarized, etc.), which is commonly achieved via local probe spectroscopy [54], and hope that these results will stimulate future experiments in that regard.

ACKNOWLEDGMENTS

The authors thank Dr. Robert Zierold for the usage of PPMS, Dr. Pai Zhao, Jun Peng, and Vincent Strenzke for their help with the experiments and critical reading, Professor Kai Rossnagel, Professor Madhu Thalakulam, Professor Tim Wehling, Professor Gabriel Bester, and Carl Nielsen for discussions and suggestions. The work was supported by PIER seed fund (CorMoS, Grant No. PIF-2021-01) and the DFG (project MEGA-JJ, Grant No. BL-487/14-1). C.H.S. acknowledges the Alexander von Humboldt Stiftung for postdoctoral research fellowship. I.G.P. acknowledges the BMBF "BMBF" project (Grant No. 05K19GU). T.S. was supported by the project No. PID2020-113164GB-I00 financed by MCIN/AEI/10.13039/501100011033, PID2020-113164GB-I00. K.W. and T.T. acknowledge support from the JSPS KAKENHI (Grants No. 19H05790, No. 20H00354, and No. 21H05233).

APPENDIX A: EXPERIMENTAL DETAILS

Sample fabrication. Commercially procured natural MoS_2 (SPI supplies) were used for our studies. We fabricate the vdW stack by dry-transfer method with poly dimethyl-siloxane (PDMS) using a homemade aligner setup. The setup has a fine rotation stage and heating to facilitate the fabrication of the twisted bilayer devices. The flakes are exfoliated from the bulk on a PDMS sheet and micropositioned and transferred to a Si/SiO_2 wafer using a home-built vdW aligner setup. During the transfer, the stage is heated to 70 °C for five minutes to reduce wrinkles and remove trapped air bubbles during the process.

A schematic showing the workflow in device fabrication is illustrated in Figs. 6(a)–6(d). First, a graphite flake (back-gate) followed by a hBN (dielectric) flake is transferred to a wafer with prefabricated contact pads, Fig. 6(a). The thickness of the hBN at the back-gate for device A is estimated to be (27 ± 3) nm from atomic force microscopy (AFM) measurements. A monolayer (bilayer) MoS_2 is transferred on top of this stack, Fig. 6(a). The twisted structures are then realized by aligning another MoS_2 flake with the edges (assumed to be zigzag) of the transferred one and then rotated employing the aligner setup to desired angle θ [Fig. 6(b)]. This second flake is then transferred on top, as illustrated in Fig. 6(c). The contacts are

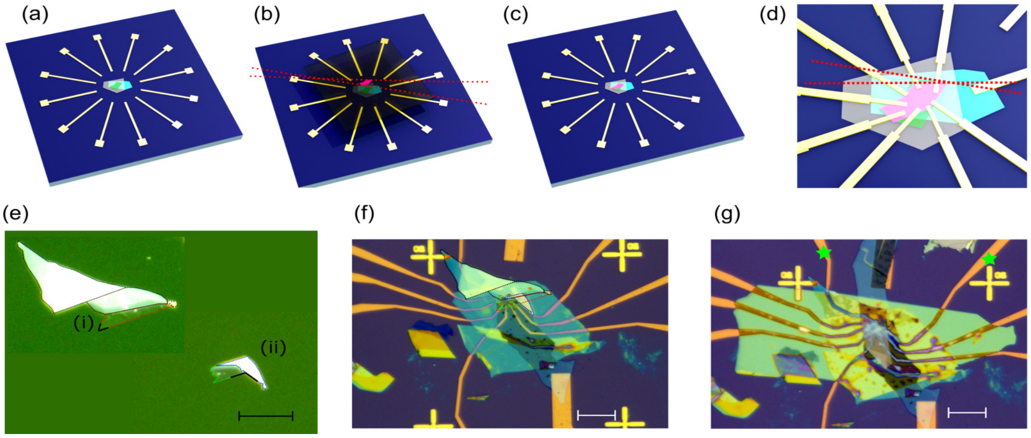

FIG. 6. (a)–(d) Schematics of the fabrication process. (a) Graphite/hBN/monolayer MoS_2 stack on Si/SiO_2 wafer (b) Second MoS_2 monolayer with edge aligned to the edge of the underlying flake and rotated to desired angle. (c) Stacked layers. (d) Zoomed view with contacts. The flakes are labeled cyan, gray, green, pink for graphite, hBN, MoS_2(i), MoS_2(ii). The dashed red lines are a guide to the eye, illustrating the relative angle between the flakes. (e) Optical images of the MoS_2 flakes on PDMS with MoS_2(i) and MoS_2(ii) on the top and bottom, respectively. (f) Optical image of the graphite/hBN/tBLM with Ti/Au contacts on top. (g) Optical image of the final device encapsulated in hBN and graphite top gate. Scale bars: 20 μm.

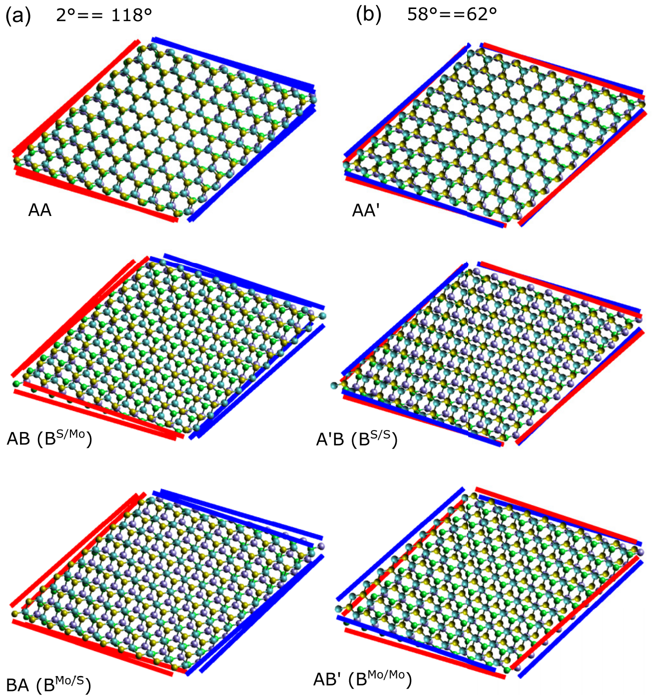

FIG. 7. Stackings for tBLM for (a) 2° and (b) 58°. The two distinct zigzag edges are marked with blue and red lines. See text for details.

made on top of the tBLM (tdBLM) using e-beam lithography and Ti/Au (5 nm/15 nm) deposition. A schematic of the contacts is shown in Fig. 6(d).

The optical images in the fabrication steps of Device A are shown in Figs. 6(e)–6(g). Figure 6(e) shows the optical images of the two MoS_2 flakes on PDMS, MoS_2(i) and MoS_2(ii) on the top and bottom, respectively. The perimeter flakes are outlined for clarity with the monolayer (bulk) regions in red and green (black and blue), respectively. Figure 6(f) shows the optical image after the contact fabrication on the tBLM. The perimeter fakes are outlined as mentioned above. Since the monolayers are not visible on the stack, we use the bulk regions (outlined in black and blue) as a guide. The twist angle is determined from the optical images. The angle between the straight edges of the monolayer regions here is measured to be $a = 4.40°$. The optical image of the final device is shown in Fig. 6(g). The device is encapsulated with another hBN flake followed by graphite as the top gate.

For the tDBLM, the same work-flow is followed except that monolayer MoS_2 is replaced by bilayer MoS_2.

Transport measurements. The devices were mounted on a chip carrier in a vacuum (2×10^{-5} mbar) probe. Device A was cooled to 4.2 K in a bath cryostat and devices B and C were cooled to 1.5 K in a variable thermal insert (VTI). All measurements were performed in the dark. Temperature-dependent measurements on device A were performed using a Quantum Design PPMS. The device was warmed and re-cooled for this measurement. The temperature dependence of device C was acquired in the VTI by regulating the helium flow and pressure in the insert. For all the measurements, a DC voltage was applied across the source-drain contacts and I_{DS} was measured using a current preamplifier. A source-measure unit was used for applying DC voltage to V_{BG} and the leakage current was monitored to ensure that no current is leaking to the gates.

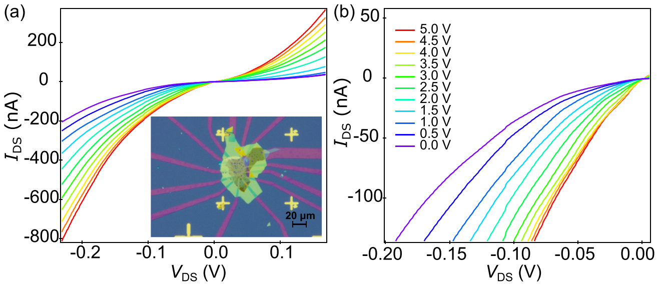

FIG. 8. (a), (b) IV characteristics of a few-layer MoS_2 device for different V_{BG} at 1.5 K. Panel (b) shows a zoom-in of the negative bias region in panel (a).

APPENDIX B: STACKING IN TWISTED MoS_2

Regions of the moiré superlattice (MSL) of MoS_2 at angles close to 0° and 60° are shown in Fig. 6. There are two distinct zigzag directions marked blue and red in Fig. 7. The blue (red) line corresponds to the zigzag where the Mo (S) atoms are outwards, we label them ZZ-Mo (ZZ-S). Although they lie parallel to each other, the alignment with respect to each other gives distinguishable moiré superlattices. ZZ-Mo (ZZ-S) aligned with ZZ-Mo (ZZ-S) will be 0° and ZZ-Mo aligned with ZZ-S will be 60° twist angle. Figures 7(a) and 7(b) shows tBLM of 2° and 58°, respectively. The Mo in the top (bottom) layer is colored blue (violet) and S in the top (bottom) is colored yellow (green). For the 2° twist [Fig. 7(a)], AA (Mo on Mo and S on S), AB (Bernal stacking with S on Mo) and BA (Bernal stacking with Mo on S) regions can be observed whereas for the 58° twist [Fig. 7(b)], AA′ stacking (Mo on S and S on Mo), A′B stacking (Bernal stacking with S on S) and AB′ (Bernal stacking with Mo on Mo) are seen. These stacking cannot be transformed into each other, making their electronic structure and hence properties different. Since ZZ-Mo and ZZ-S are optically indistinguishable, aligning the straight edges will give us a twist angle of a or $60° - a$. Thus,

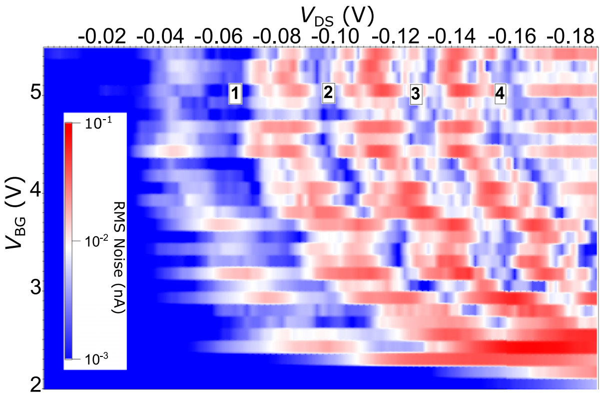

FIG. 9. Root mean square extracted noise from the data in Fig. 3(c).

the twist angle of our tBLM device could be $a = 4.40^\circ$ or $a' = 55.6^\circ$.

APPENDIX C: *I-V* CHARACTERISTICS FOR A FEW-LAYER MoS$_2$ DEVICE

The *I-V* characteristics at 1.5 K for different gate voltages of a few-layer MoS$_2$ device sandwiched in hBN and graphite gates in Fig. 8 show a monotonic behavior. The device fabrication and measurement methods are identical to that of the devices (Devices A, B, and C) described in the main text except for the MSL. The nonlinear *I-V* characteristics due to the Schottky contacts can be seen here as well.

APPENDIX D: NOISE SPECTRUM IN DEVICE A

To quantify the noise, we compute the root-mean-square (rms) deviation of the averaged current on regular gate intervals. The result is shown in Fig. 9. We identify the plateau regions (1–4) where the noise is low (blue). In between these regions, the noise increases (red).

[1] Y. Cao, V. Fatemi, A. Demir, S. Fang, S. L. Tomarken, J. Y. Luo, J. D. Sanchez-Yamagishi, K. Watanabe, T. Taniguchi, E. Kaxiras, R. C. Ashoori, and P. Jarillo-Herrero, Correlated insulator behaviour at half-filling in magic-angle graphene superlattices, Nature (London) **556**, 80 (2018).

[2] Y. Cao, V. Fatemi, S. Fang, K. Watanabe, T. Taniguchi, E. Kaxiras, and P. Jarillo-Herrero, Unconventional superconductivity in magic-angle graphene superlattices, Nature (London) **556**, 43 (2018).

[3] M. Yankowitz, S. Chen, H. Polshyn, Y. Zhang, K. Watanabe, T. Taniguchi, D. Graf, A. F. Young, and C. R. Dean, Tuning superconductivity in twisted bilayer graphene, Science **363**, 1059 (2019).

[4] A. L. Sharpe, E. J. Fox, A. W. Barnard, J. Finney, K. Watanabe, T. Taniguchi, M. A. Kastner, and D. Goldhaber-Gordon, Emergent ferromagnetism near three-quarters filling in twisted bilayer graphene, Science **365**, 605 (2019).

[5] M. Serlin, C. L. Tschirhart, H. Polshyn, Y. Zhang, J. Zhu, K. Watanabe, T. Taniguchi, L. Balents, and A. F. Young, Intrinsic quantized anomalous Hall effect in a moiré; heterostructure, Science **367**, 900 (2020).

[6] R. Bistritzer and A. H. MacDonald, Moiré bands in twisted double-layer graphene, Proc. Natl. Acad. Sci. USA **108**, 12233 (2011).

[7] X. Cai, L. An, X. Feng, S. Wang, Z. Zhou, Y. Chen, Y. Cai, C. Cheng, X. Pan, and N. Wang, Layer-dependent interface reconstruction and strain modulation in twisted WSe$_2$, Nanoscale **13**, 13624 (2021).

[8] L. Wang, E.-M. Shih, A. Ghiotto, L. Xian, D. A. Rhodes, C. Tan, M. Claassen, D. M. Kennes, Y. Bai, B. Kim, K. Watanabe, T. Taniguchi, X. Zhu, J. Hone, A. Rubio, A. N. Pasupathy, and C. R. Dean, Correlated electronic phases in twisted bilayer transition metal dichalcogenides, Nat. Mater. **19**, 861 (2020).

[9] F. Wu, T. Lovorn, E. Tutuc, and A. H. Macdonald, Hubbard model physics in transition metal dichalcogenide moiré bands, Phys. Rev. Lett. **121**, 026402 (2018).

[10] H. Pan, F. Wu, and S. Das Sarma, Band topology, Hubbard model, Heisenberg model, and Dzyaloshinskii-Moriya interaction in twisted bilayer WSe$_2$, Phys. Rev. Res. **2**, 033087 (2020).

[11] T. Devakul, V. Crépel, Y. Zhang, and L. Fu, Magic in twisted transition metal dichalcogenide bilayers, Nat. Commun. **12**, 6730 (2021).

[12] M. H. Naik and M. Jain, Ultraflatbands and shear solitons in moiré patterns of twisted bilayer transition metal dichalcogenides, Phys. Rev. Lett. **121**, 266401 (2018).

[13] M. H. Naik, S. Kundu, I. Maity, and M. Jain, Origin and evolution of ultraflat bands in twisted bilayer transition metal dichalcogenides: Realization of triangular quantum dots, Phys. Rev. B **102**, 075413 (2020).

[14] L. Xian, M. Claassen, D. Kiese, M. M. Scherer, S. Trebst, D. M. Kennes, and A. Rubio, Realization of nearly dispersionless bands with strong orbital anisotropy from destructive interference in twisted bilayer MoS$_2$, Nat. Commun. **12**, 5644 (2021).

[15] Y. Tang, L. Li, T. Li, Y. Xu, S. Liu, K. Barmak, K. Watanabe, T. Taniguchi, A. H. MacDonald, J. Shan, and K. F. Mak, Simulation of Hubbard model physics in WSe$_2$/WS$_2$ moiré superlattices, Nature (London) **579**, 353 (2020).

[16] Y. Lemonik, I. L. Aleiner, C. Toke, and V. I. Fal'ko, Spontaneous symmetry breaking and Lifshitz transition in bilayer graphene, Phys. Rev. B **82**, 201408(R) (2010).

[17] U. Zondiner, A. Rozen, D. Rodan-Legrain, Y. Cao, R. Queiroz, T. Taniguchi, K. Watanabe, Y. Oreg, F. von Oppen, A. Stern, E. Berg, P. Jarillo-Herrero, and S. Ilani, Cascade of phase transitions and Dirac revivals in magic-angle graphene, Nature (London) **582**, 203 (2020).

[18] S. C. de la Barrera, S. Aronson, Z. Zheng, K. Watanabe, T. Taniguchi, Q. Ma, P. Jarillo-Herrero, and R. Ashoori, Cascade of isospin phase transitions in Bernal-stacked bilayer graphene at zero magnetic field, Nat. Phys. **18**, 771 (2022).

[19] D. Wong, K. P. Nuckolls, M. Oh, B. Lian, Y. Xie, S. Jeon, K. Watanabe, T. Taniguchi, B. A. Bernevig, and A. Yazdani, Cascade of electronic transitions in magic-angle twisted bilayer graphene, Nature (London) **582**, 198 (2020).

[20] K. Marinov, A. Avsar, K. Watanabe, T. Taniguchi, and A. Kis, Resolving the spin splitting in the conduction band of monolayer MoS$_2$, Nat. Commun. **8**, 1938 (2017).

[21] K. F. Mak, C. Lee, J. Hone, J. Shan, and T. F. Heinz, Atomically thin MoS$_2$: A new direct-gap semiconductor, Phys. Rev. Lett. **105**, 136805 (2010).

[22] Y. Guo, C. Liu, Q. Yin, C. Wei, S. Lin, T. B. Hoffman, Y. Zhao, J. H. Edgar, Q. Chen, S. P. Lau, J. Dai, H. Yao, H. S. Wong, and Y. Chai, Distinctive in-plane cleavage behaviors of two-dimensional layered materials, ACS Nano **10**, 8980 (2016).

[23] X. Wang, A. Tabarraei, and D. E. Spearot, Fracture mechanics of monolayer molybdenum disulfide, Nanotechnol. **26**, 175703 (2015).

[24] N. Kaushik, A. Nipane, F. Basheer, S. Dubey, S. Grover, M. M. Deshmukh, and S. Lodha, Schottky barrier heights for Au and Pd contacts to MoS$_2$, Appl. Phys. Lett. **105**, 113505 (2014).

[25] C. Gong, L. Colombo, R. M. Wallace, and K. Cho, The unusual mechanism of partial Fermi level pinning at metal-MoS_2 interfaces, Nano Lett. **14**, 1714 (2014).

[26] H. Zhou, L. Holleis, Y. Saito, L. Cohen, W. Huynh, C. L. Patterson, F. Yang, T. Taniguchi, K. Watanabe, and A. F. Young, Isospin magnetism and spin-polarized superconductivity in Bernal bilayer graphene, Science **375**, 774 (2022).

[27] Y. Cao, D. Rodan-Legrain, O. Rubies-Bigorda, J. M. Park, K. Watanabe, T. Taniguchi, and P. Jarillo-Herrero, Tunable correlated states and spin-polarized phases in twisted bilayer-bilayer graphene, Nature (London) **583**, 215 (2020).

[28] X. Liu, Z. Hao, E. Khalaf, J. Y. Lee, Y. Ronen, H. Yoo, D. Haei Najafabadi, K. Watanabe, T. Taniguchi, A. Vishwanath, and P. Kim, Tunable spin-polarized correlated states in twisted double bilayer graphene, Nature (London) **583**, 221 (2020).

[29] H. Zhou, T. Xie, A. Ghazaryan, T. Holder, J. R. Ehrets, E. M. Spanton, T. Taniguchi, K. Watanabe, E. Berg, M. Serbyn, and A. F. Young, Half- and quarter-metals in rhombohedral trilayer graphene, Nature (London) **598**, 429 (2021).

[30] H. Rostami, A. G. Moghaddam, and R. Asgari, Effective lattice Hamiltonian for monolayer MoS_2: Tailoring electronic structure with perpendicular electric and magnetic fields, Phys. Rev. B **88**, 085440 (2013).

[31] I. Paradisanos, S. Shree, A. George, N. Leisgang, C. Robert, K. Watanabe, T. Taniguchi, R. J. Warburton, A. Turchanin, X. Marie, I. C. Gerber, and B. Urbaszek, Controlling interlayer excitons in MoS_2 layers grown by chemical vapor deposition, Nat. Commun. **11**, 2391 (2020).

[32] Z. Gong, G.-B. Liu, H. Yu, D. Xiao, X. Cui, X. Xu, and W. Yao, Magnetoelectric effects and valley-controlled spin quantum gates in transition metal dichalcogenide bilayers, Nat. Commun. **4**, 2053 (2013).

[33] T. Stauber, P. San-Jose, and L. Brey, Optical conductivity, Drude weight and plasmons in twisted graphene bilayers, New J. Phys. **15**, 113050 (2013).

[34] N. N. T. Nam and M. Koshino, Lattice relaxation and energy band modulation in twisted bilayer graphene, Phys. Rev. B **96**, 075311 (2017).

[35] M. Koshino, N. F. Q. Yuan, T. Koretsune, M. Ochi, K. Kuroki, and L. Fu, Maximally localized Wannier orbitals and the extended Hubbard model for twisted bilayer graphene, Phys. Rev. X **8**, 031087 (2018).

[36] J. Gonzalez and T. Stauber, Ising superconductivity induced from valley symmetry breaking in twisted trilayer graphene, Nat. Commun. **14**, 2746 (2023).

[37] A. Laturia, M. L. Van de Put, and W. G. Vandenberghe, Dielectric properties of hexagonal boron nitride and transition metal dichalcogenides: From monolayer to bulk, npj 2D Mater. Appl. **2**, 6 (2018).

[38] J. M. B. Lopes dos Santos, N. M. R. Peres, and A. H. Castro Neto, Graphene bilayer with a twist: Electronic structure, Phys. Rev. Lett. **99**, 256802 (2007).

[39] E. J. Miller, E. T. Yu, P. Waltereit, and J. S. Speck, Analysis of reverse-bias leakage current mechanisms in GaN grown by molecular-beam epitaxy, Appl. Phys. Lett. **84**, 535 (2004).

[40] J. H. Davies, *The Physics of Low-dimensional Semiconductors* (Cambridge University Press, Cambridge, 1997).

[41] L. S. Yu, Q. Z. Liu, Q. J. Xing, D. J. Qiao, S. S. Lau, and J. Redwing, The role of the tunneling component in the current-voltage characteristics of metal-GaN Schottky diodes, J. Appl. Phys. **84**, 2099 (1998).

[42] G. Breit and E. Wigner, Capture of slow neutrons, Phys. Rev. **49**, 519 (1936).

[43] C. W. J. Beenakker, Theory of Coulomb-blockade oscillations in the conductance of a quantum dot, Phys. Rev. B **44**, 1646 (1991).

[44] I. Maity, M. H. Naik, P. K. Maiti, H. R. Krishnamurthy, and M. Jain, Phonons in twisted transition-metal dichalcogenide bilayers: Ultrasoft phasons and a transition from a superlubric to a pinned phase, Phys. Rev. Res. **2**, 013335 (2020).

[45] L.-N. Nguyen, Y.-W. Lan, J.-H. Chen, T.-R. Chang, Y.-L. Zhong, H.-T. Jeng, L.-J. Li, and C.-D. Chen, Resonant tunneling through discrete quantum states in stacked atomic-layered MoS_2, Nano Lett. **14**, 2381 (2014).

[46] M. A. Reed, J. N. Randall, R. J. Aggarwal, R. J. Matyi, T. M. Moore, and A. E. Wetsel, Observation of discrete electronic states in a zero-dimensional semiconductor nanostructure, Phys. Rev. Lett. **60**, 535 (1988).

[47] L. Esaki and R. Tsu, Superlattice and negative differential conductivity in semiconductors, IBM J. Res. Dev. **14**, 61 (1970).

[48] S. Ishigaki and S. Nakamura, Mechanism for negative differential conductivity in holographic conductors, J. High Energy Phys. 12 (2020) 124.

[49] M. Shin, S. Lee, K. W. Park, and E.-H. Lee, Additional Coulomb blockade and negative differential conductance in closed two-dimensional tunnel junction arrays, J. Appl. Phys. **84**, 2974 (1998).

[50] V. H. Nguyen, V. L. Nguyen, and H. N. Nguyen, Coulomb blockade and negative differential conductance in metallic double-dot devices, J. Appl. Phys. **96**, 3302 (2004).

[51] L. Balents, C. R. Dean, D. K. Efetov, and A. F. Young, Superconductivity and strong correlations in moiré flat bands, Nat. Phys. **16**, 725 (2020).

[52] S. Das and J. Appenzeller, Where does the current flow in two-dimensional layered systems? Nano Lett. **13**, 3396 (2013).

[53] C. E. M. Nielsen, M. Da Cruz, A. Torche, and G. Bester, Accurate force-field methodology capturing atomic reconstructions in transition metal dichalcogenide moiré system, Phys. Rev. B **108**, 045402 (2023).

[54] K. P. Nuckolls, R. L. Lee, M. Oh, D. Wong, T. Soejima, J. P. Hong, D. Călugăru, J. Herzog-Arbeitman, B. A. Bernevig, K. Watanabe, T. Taniguchi, N. Regnault, M. P. Zaletel, and A. Yazdani, Quantum textures of the many-body wavefunctions in magic-angle graphene, Nature (London) **620**, 525 (2023).